Multi-pass serpentine flow-fields to enhance under-rib convection in polymer electrolyte membrane fuel cells: Design and geometrical characterization

Jin Hyun Nam [a],*, Kyu-Jin Lee [b], Sangho Sohn [b], Charn-Jung Kim [b]

[a] *School of Mechanical and Automotive Engineering, Kookmin University, Seoul 136-702, Republic of Korea*
[b] *School of Mechanical and Aerospace Engineering, Seoul National University, Seoul 151-744, Republic of Korea*

ABSTRACT

The flow-field for reactant distribution is an important design factor that influences the performance of polymer electrolyte membrane fuel cells (PEMFCs). Under-rib convection between neighboring channels has been recognized to enhance the performance of PEMFCs with serpentine flow-fields. This study presents a simple design method to generate multi-pass serpentine flow-fields (MPSFFs) that can maximize under-rib convection in a given cell area. Geometrical characterization indicates that MPSFFs lead to significantly higher under-rib convection intensities and more uniform conditions, such as reactant concentrations, temperature, and liquid water saturation, compared with conventional serpentine flow-fields. The implications of the enhanced under-rib convection due to MPSFFs on the performance of PEMFCs are discussed.

© 2008 Elsevier B.V. All rights reserved.

1. Introduction

Fuel cells produce fewer harmful emissions and are more efficient compared with heat engines (Carnot efficiency) by directly converting the chemical energy of fuels into electricity without combustion [1,2]. In addition, fuel cells can overcome the drawbacks of present rechargeable batteries by providing longer operation time and instant refuelling features. Thus, fuel cells are expected to serve as important power sources in many applications in the near future. Among the many types of fuel cell, polymer electrolyte membrane fuel cells (PEMFCs) have been applied to a diverse variety of uses that, include portable, automobile and stationary power generation. The relatively low operating temperature of PEMFCs, i.e. below 100 °C enables fast start-up at the beginning phase and good dynamic response to load change. These excellent transient characteristics of PEMFCs are essential for applications that require short-term repeated operations. Currently, much effort is being applied to develop more efficient PEMFCs that are able to operate at higher current densities.

The performance of a PEMFC is primarily determined by the intrinsic electrochemical efficiency of the membrane electrode assembly (MEA). Nevertheless, other factors, such as flow-field design, thermal and water management, and operational control are also important [3]. Accordingly, many workers have investi-gated viable flow-field designs suitable for PEMFCs [4]. Three basic type of flow-field are commonly used for PEMFCs, namely, parallel, serpentine and interdigitated flow-fields. The parallel version is the simplest and requires the smallest pressure drop by equally distributing the flow rate into many straight parallel paths. On the other hand, non-uniform distribution of the reactant gas between paths can occur in parallel flow-fields if the flow resistance of each path is not maintained at a comparable level. Serpentine flow-field designs have been proposed to solve the maldistribution problem inherent to parallel flow-fields by forcing the reactant gas to flow through a single, long, meandering path that travels over the entire active area. Thus, the flow speed and the pressure drop in serpentine flow-fields are both very high, which also facilitates a two-phase transport of liquid water droplets through the gas channels of PEM-FCs.

Interdigitated flow-fields are based on dead-end channel designs, which direct reactant gases to flow through porous gas diffusion layers (GDLs) by under-rib paths [5,6]. The presence of a convective flow in the under-rib regions enables more effective utilization of electrocatalysts by increasing reactant concentration and facilitating liquid water removal in those regions. This under-rib convection has recently been recognized by many researchers [7–17] as a non-negligible transport process that influences the performance of PEMFCs and direct methanol fuel cells (DMFCs) with serpentine flow-fields. Experimental studies have shown that higher GDL permeability improves the performance of PEMFCs with serpentine flow-fields [8,9] and reduces the pressure drop [16]. Pharoah [10] observed that under-rib convection can not be ignored when GDL permeability exceeds 10^{-13} m^2, which is consistent with

* Corresponding author at: 861-1 Jeongneung-dong, Seongbuk-gu, Seoul 136-702, Republic of Korea. Tel.: +82 2 910 4858; fax: +82 2 910 4839.
E-mail address: akko2@kookmin.ac.kr (J.H. Nam).

the analytical model prediction for the relative influence of under-rib convection [13]. The role of under-rib convection in DMFCs was also numerically studied by Ye et al. [14].

Recently, Xu and Zhao [18] proposed a new flow-field design for polymer-based fuel cells, namely, the convection enhanced serpentine flow-field (CESFF). They experimentally showed that a small DMFC (3 cm × 3 cm) with a CESFF could perform better and more stably than a similar DMFC with a conventional serpentine flow-field, especially at smaller air flow rates. They attributed the enhanced performance to the ability of the CESFF to handle liquid water in the under-rib regions. Similar flow-field designs have also been proposed as coolant flow-fields for PEMFCs [19,20]. By placing flow channels of different path-lengths (the travelled distance from an inlet) near one another, an improved temperature uniformity in the cooling plate was numerically predicted. It should be noted that uniform temperature is also favourable for the operation control and the long-term durability of PEMFCs. The idea of close placement of flow-channels with different path-lengths was previously proposed by Kaufman and Terry [21]. Later, Qi and Kaufman [22] demonstrated that a PEMFC with a double-path (counter-flow) cathode flow-field could operate stably under low-humidity conditions when using dry reactant gases. They reported that the double-path-type flow-field facilitated the humidification of dry entering gases with internally produced water.

Based on previous studies [18–22], multi-pass serpentine flow-fields (MPSFFs) are proposed in this study to enhance the under-rib convection and thus improve the performance of PEMFCs. The MPSFFs cause reactant gases to travel mutiple timer between the region near an inlet and that near an outlet and thereby results in closely-interlaced channels with widely different path-lengths. The channel patterns in MPSFFs are believed to enable higher under-rib convection, more uniform concentration distribution, and fast exhaust of liquid water from the under-rib regions. This study presents a step-by-step design to generate MPSFFs, along with several exemplary flow-fields, i.e., single-path MPSFFs for a small active area of 9 cm² (3 cm × 3 cm) and parallel-path MPSFFs for a relatively large active area of 81 cm² (9 cm × 9 cm). Next, the geometrical characterization is presented for those exemplary single- and parallel-path MPSFFs and is based on the channel path-length distribution in the active area. Finally, the effects of under-rib convection enhancement by MPSFFs on the overall performance of PEMFCs are discussed in relation to influence of cell size.

2. Theory and calculations

2.1. Under-rib convection mechanism

The mechanism of under-rib convection is explained with three neighbouring channel regions A, B, and C in the exemplary (3-pass) serpentine flow-field shown in Fig. 1(a). The path-lengths Z_A, Z_B, and Z_C are defined as the distance travelled by the reactant gas from an inlet to the three regions along the channel—illustrated by dotted lines in Fig. 1(a). The path-length, z, can be viewed as a coordinate whose upper limit is the same as the total length of the path, z_{max}. The pressure and the reactant concentration in PEMFCs are expected to change linearly along the flow channel, i.e., with respect to z.

The total flow rate, q_{tot}, depends on the total pressure drop, Δp_{tot}, across the flow-field as espressed by [23]:

$$q_{tot} = \frac{K_{ch}}{\mu} A_{ch} \frac{\Delta p_{tot}}{z_{max}}, \qquad (1)$$

where: μ is the viscosity; A_{ch} is the cross-sectional area of the channel (height h_{ch} × width w_{ch}); K_{ch} is the channel permeability derived from the Hagen-Poiseuille equation. Note that Eq. (1) assumes that the flow rate is constant along the channel with a low
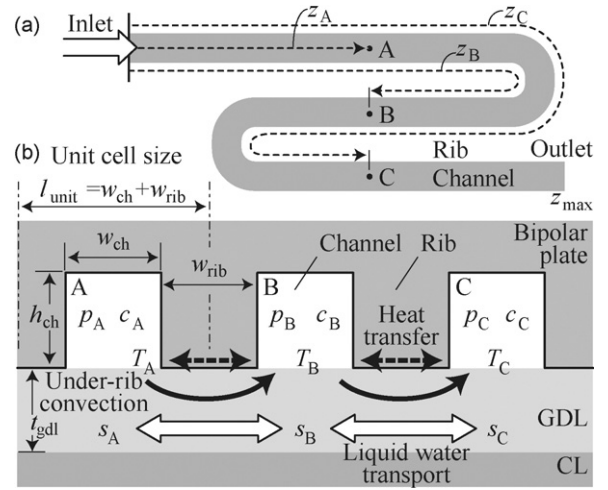

Fig. 1. Under-rib convection and transport in serpentine flow-field: (a) definition of path-length, z; (b) under-rib convection and transport mechanisms.

under-rib convection flow rate ($q_{rib} \approx 0$), and that the secondary (non-linear) pressure loss in 90° or 180° corners is negligible. Thus, the permeability, K_{ch}, is determined by [24]:

$$K_{ch} = \frac{h_{ch}^2}{28.45}, \qquad (2)$$

from the Darcy friction factor of $f = 56.9/Re$ for square channels. In this study, K_{ch} is estimated to be 3.515×10^{-8} m² for square-channel geometry with $h_{ch} = w_{ch} = 1$ mm. The pressure difference between two neighbouring channel regions is expressed in terms of the path-length difference as:

$$|p_A - p_B| = \frac{\Delta p_{tot}}{z_{max}} |z_A - z_B| = \frac{q_{tot}\mu}{K_{ch}A_{ch}} |z_A - z_B|. \qquad (3)$$

Let us assume that the flow-field shown in Fig. 1(a) is for the cathode of an PEMFC. The reactant concentration, c (mol m⁻³), then denotes the molar concentration of oxygen, and the total concentration loss, $\Delta c_{tot} = c_{in} - c_{out}$, across the flow-field is calculated from the mass balance of oxygen as according to:

$$(c_{in} - c_{out})q_{tot} = \Delta c_{tot} q_{tot} = \frac{I_{tot}}{4F} \qquad (4)$$

Here, I_{tot} (A) is the current generated over the entire cell area and F is the Faraday constant (96487 C mol⁻¹). Note that Eq. (4) ignores the change in the total flow rate, q_{tot}, due to oxygen consumption. In fact, the reactant flow rate in the cathode is relatively constant because the humidified air (with an oxygen mole fraction of about 0.15) is supplied at high excess air ratios. If current is generated uniformly throughout the active area, the concentration difference between two neighbouring channel regions is also expressed in terms of the path-length difference, i.e.,

$$|c_A - c_B| = \frac{\Delta c_{tot}}{z_{max}} |z_A - z_B| = \frac{I_{tot}}{4Fq_{tot}z_{max}} |z_A - z_B| \qquad (5)$$

Fig. 1(b) shows the cross-sectional view of the three adjacent channel regions A, B, and C. Region A has the highest pressure and reactant concentration, while region C has the lowest among the regions ($p_A > p_B > p_C$ and $c_A > c_B > c_C$). Due to the pressure difference between neighbouring regions, convective flow occurs through under-rib regions in the GDL, as shown in Fig. 1(b). This additional convective flow through GDLs is called the under-rib convection, and is believed to improve the performance of PEMFCs. Under-rib convection increases the reactant concentration in the under-rib regions, facilitates liquid water removal from those regions, and enables a more uniform concentration distribution throughout the

flow-fields. The under-rib convection flow rate, q_{rib}, is proportional to the pressure difference between two neighbouring regions. For example, q_{rib}^{AB} between regions A and B in Fig. 1(b) can be expressed as [23]:

$$q_{rib}^{AB} = \frac{K_{gdl}}{\mu} A_{rib}^{AB} \frac{|p_A - p_B|}{w_{rib}} = q_{tot} \frac{K_{gdl} A_{rib}}{K_{ch} A_{ch}} \frac{|z_A - z_B|}{w_{rib}}, \qquad (6)$$

where K_{gdl} is the flow permeability of the GDL, w_{rib} is the rib width, and A_{rib}^{AB} is the flow area for the under-rib convection. Note that A_{rib}^{AB} is determined by multiplying the GDL thickness, t_{gdl}, and some length, l_{ch}, of the regions along the channel (the under-rib convection through the catalyst layer is ignored).

Fig. 1(b) shows that other transport mechanisms also become active when channel regions that have different path-lengths are in close contact. The local temperature and liquid water saturation in GDLs depend on the electrochemical reaction rate, and this is generally governed by the reactant concentration, which varies along the channel (with respect to z). The temperature gradient due to closely placed channels of different path-lengths facilitates conductive heat transfer by the under-rib or cross-rib paths, and the water saturation gradient facilitates capillary transport of water by the under-rib path. These transport mechanisms may be termed as under-rib transports to distinguish them from under-rib convection. While under-rib convection occurs in only one direction (from a high-pressure region towards a low-pressure region), under-rib transports may occur in both directions, as shown in Fig. 1(b). In fact, Qi and Kaufman [22] attributed the successful dry operation of their PEMFC to the under-rib transport of water in the opposite direction of the under-rib convection. Thus, under-rib convection and transport are believed to enhance the uniformity of operation conditions in the flow-fields, including the reactant and product concentrations, temperature and liquid water saturation, as shown in Fig. 1(b).

2.2. Geometrical characterization

The two unit cells used for the generation and characterization of flow-fields are presented in Fig. 2(a). The unit cell length, l_{unit}, is defined as the sum of the channel width, w_{ch}, and the rib width,

Fig. 2. Geometrical characterization of flow-fields: (a) unit channel cells; (b) definitions of path-length difference, Δz, and local-averaged path-length, $\bar{z}$.

w_{rib}, in Fig. 1(b). Thus, l_{unit} is 2 mm in this study, while both w_{ch} and w_{rib} are assumed to be 1 mm. It should be noted that any serpentine flow-field for PEMFCs can be constructed by paving the active area with channel cells that have been chosen from the two unit cells and then rotated properly.

A channel cell generally has two neighbouring channel cells connected through the under-rib regions, which is indicated by the double-headed arrows in Fig. 2(a). The channel cells located at the edge of the flow-field may have no or only one neighboring channel cell. The path-length difference, Δz_i, of a unit cell i is determined by summing the absolute difference of the path-length z between the cell i and each neighbouring cell j, or

$$\Delta z_i = \sum_{j=\text{neighboring channels of } i} |z_i - z_j| \qquad (7)$$

The calculation procedures for Δz_i of the channel cells A, B, and C are shown in Fig. 2(b). The Δz_i is a good geometrical index for measurement of the under-rib convection in a flow-field, as explained by Eq. (6).

The local-averaged path-length, $\bar{z}$, described in Fig. 2(b) is another good geometrical index for measuring the uniformity of local conditions in a flow-field. Conditions such as the reactant and product concentrations, temperature and liquid water saturation, generally vary along the channel (with respect to z). The $\bar{z}_i$ of a unit channel cell i is calculated by averaging its path-length with those of adjacent channel cells j. A 3×3 averaging mask (a dotted box in Fig. 2(b)) consisting of nine adjacent cells is used to determine $\bar{z}_i$ as:

$$\bar{z}_i = \frac{1}{n_{avg}} \sum_{j=\text{adjacent channels of } i} z_j, \qquad (8)$$

where n_{avg} is the number of adjacent cells used for the local averaging. Thus, n_{avg} is nine for most channel cells, but for channel cells located at the edge of the flow-field, a n_{avg} of six or four should be used, as shown in Fig. 2(b).

A small standard deviation, σ_z, of the local-averaged path-length, $\bar{z}$, from its average of $(\bar{z})_{avg} = z_{max}/2$, is desirable to obtain more uniform operational conditions in the entire active area. In addition, the distribution of $\bar{z}$ can be used to estimate the performance of cooling plates for PEMFCs because the temperature of a cooling fluid increases rather linearly with z [19,20].

2.3. Under-rib convection intensity

The under-rib convection intensity can be assessed by comparing the under-rib convection flow rate, q_{rib}, and the total flow rate across the flow-field, q_{tot}. This approach has been previously used to evaluate the under-rib convection in serpentine flow-fields [10–13,18]. In the MPSFFs proposed in this study, the first one-third of the path-length of the channel region ($z < z_{max}/3$) generally contacts with a channel region with a larger path-length ($z > z_{max}/3$). Thus, the reactant flow rate along the channel q_{ch} almost always decreases for $z < z_{max}/3$ due to the under-rib convection in MPSFFs.

In this study, the under-rib convection intensity is defined as the ratio of the under-rib convection flow rate, $q_{rib,1/3}$, for the first one-third of path-length ($z < z_{max}/3$) to the total flow rate, q_{tot}. By setting A_{rib} in Eq. (6) as $z_{max} t_{gdl}/3$, the under-rib convection intensity $q_{rib,1/3}/q_{tot}$ is determined as:

$$\frac{q_{rib,1/3}}{q_{tot}} = \frac{1}{3} \frac{K_{gdl} t_{gdl} z_{max}}{K_{ch} h_{ch} w_{ch}} \frac{(\Delta z)_{avg,1/3}}{w_{rib}}, \qquad (9)$$

where $(\Delta z)_{avg,1/3}$ is the average path-length difference for the first 1/3 path-length of the flow-field. Eq. (9) clearly shows that the under-rib convection intensity depends on the maximum path-length, z_{max}, and therefore indicates that cell size is an important factor in determining the under-rib convection intensity. Although
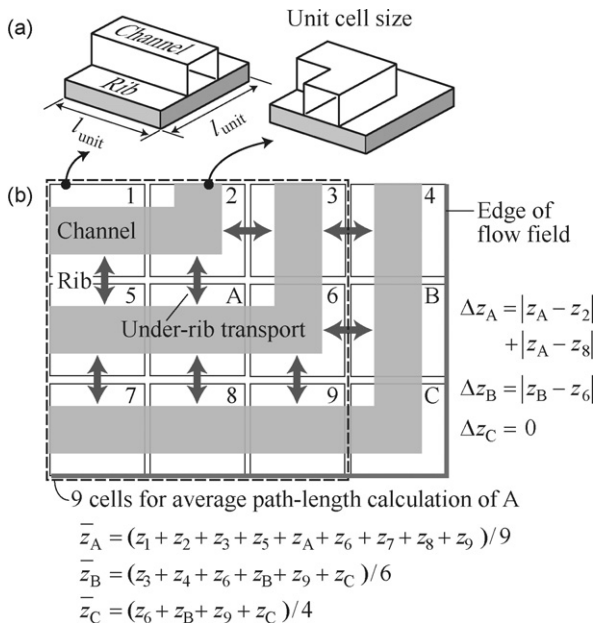
Table 1
Geometrical parameters for generating MPSFFs and estimating their under-rib convection intensities.

Parameter	Explanation	Value
h_{ch}	Channel height	1 mm
w_{ch}	Channel width	1 mm
w_{rib}	Rib width	1 mm
t_{gdl}	GDL thickness	0.2 mm
K_{ch}	Channel permeability	3.515×10^{-8} m^2
K_{gdl}	GDL permeability	1.0×10^{-12} m^2

Eq. (9) allows an easy comparison of the under-rib convection intensities in different flow-fields, it only gives approximate values because a small under-rib convection is assumed in its derivation.

Geometrical parameters for estimating the under-rib convection intensities of MPSFFs are summarized in Table 1. The GDL permeability, K_{gdl}, is assumed to be 1×10^{-12} m^2 in this study. The permeabilities of different GDL materials for PEMFCs have been measured by several researchers [8,25,26]. Williams et al. [8] reported the through-plane permeability of several GDL materials, and obtained 8.7×10^{-12} m^2 for a bare Toray carbon paper (TGP-H-120) with 75.6% porosity, and 1.9×10^{-12} m^2 for the same paper after a microporous layer application. Similarly, Feser et al. [26] showed that the in-plane permeability of a Toray carbon paper (TGP-H-60) amounts to about 5×10^{-12} m^2 for 70% porosity. Considering the reduction of pore volume in GDL materials due to hydrophobic coating and compression, the assumed GDL permeability of 1×10^{-12} m^2 seems to be reasonable. In addition, the presence of liquid water in GDLs during PEMFC operation further reduces the gas-phase permeability due to two-phase flow effects.

3. Results

3.1. Basic channel patterns

Fig. 3(a) depicts several basic channel patterns denoted according to the number of passes, n_{pass}. All of the channel patterns except
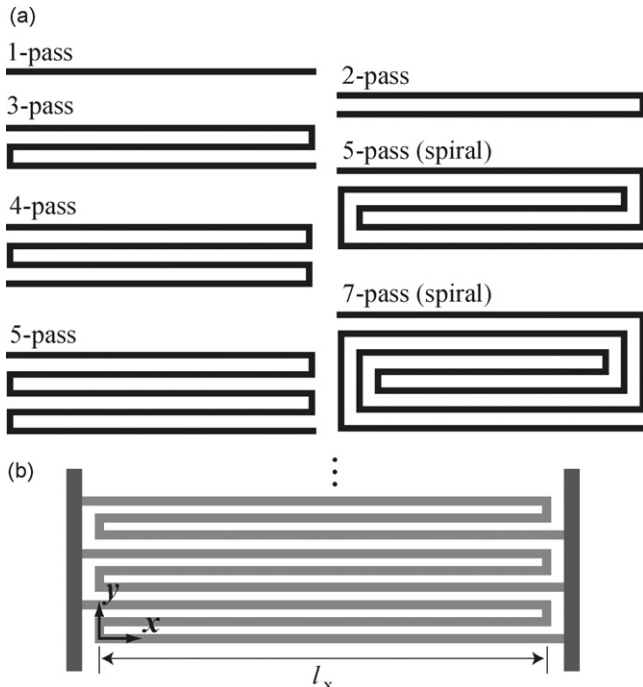

Fig. 3. Construction of basic parallel flow-fields: (a) basic multi-pass channel patterns; (b) parallel arrangement of 3-pass channel patterns.

for the 1-pass pattern force the reactant gas to travel between the inlet region and the outlet region multiple times. This multi-pass flow structure incurs closely-interlaced channels of widely different path-lengths—which are essential for constructing the multi-pass serpentine flow-fields (MPSFFs) proposed in this study. Therefore, the basic channel patterns shown in Fig. 3(a) serve as the elementary building blocks for generating single- or parallel-path MPSFFs. Fig. 3(b) shows an exemplary parallel flow-field that is constructed by arranging the 3-pass patterns. Such parallel flow-fields are considered first because they have relatively simple geometries suitable for characterizing the basic channel patterns.

The 1-pass pattern does not produce a multi-pass flow structure when arranged in parallel, but instead, serves as a reference corresponding to conventional parallel flow-fields with negligible under-rib convection. The 2-pass pattern is the simplest among the multi-pass channel patterns, and is also expected to lead to the highest under-rib convection intensity. The 2-pass pattern does not, however easily generate parallel flow-fields because the inlet and outlet ports must be made on the same side of the cell area. In fact, any basic channel pattern having an even number of passes, i.e., the 2- and 4-pass patterns in Fig. 3(a), is not suitable for constructing parallel-path MPSFFs. The 3-pass pattern is the simplest among the basic patterns with odd numbers of passes, and is also suitable for both single- and parallel-path MPSFF construction.

The 4-pass and 5-pass channel patterns shown in Fig. 3(a) generally result in a smaller path-length difference than that of the 2-pass or 3-pass patterns, and thus, are not suitable for maximizing the under-rib convection. Therefore, the 4-pass and 5-pass channel patterns depicted in Fig. 3(a) were not considered for the generation and geometrical characterization of MPSFFs in this study. Nevertheless these patterns may be useful when it is necessary to control excessive under-rib convection in MPSFFs. Two spiral channel patterns, denoted as the 5-pass (spiral) and 7-pass (spiral), are shown in Fig. 3(a), and exhibit a close geometrical similarity to the 2-pass pattern. In fact, the spiral patterns generally lead to very high under-rib convection in MPSFFs, similar to the 2-pass pattern. It should be noted that the maximum path-length in MPSFFs tends to be too large as the pass number increases, which renders basic channel patterns with larger pass numbers less useful.

Fig. 4 shows the distributions of the path-length difference, Δz, and the local-averaged path-length, $\bar{z}^{y\parallel}$, in parallel flow-fields constructed using the basic 1-pass, 2-pass, 3-pass, 5-pass (spiral), and 7-pass (spiral) patterns. The $\bar{z}^{y\parallel}$ in Fig. 4(b) is calculated by averaging the path-lengths of infinitely many channels in the y-direction. Fig. 4(a) shows that the 1-pass and 2-pass patterns set the lower and the upper boundaries between which Δz lies.

$$\text{Lower boundary}: \ \Delta z = 0. \tag{10}$$

$$\begin{aligned} \text{Upper boundary}: \ \Delta z &= 2z_{max}\left(\frac{1-2z}{z_{max}}\right) \text{ for } z < \frac{z_{max}}{2}, \\ \Delta z &= 2z_{max}\left(\frac{2z}{z_{max}-1}\right) \text{ for } z > \frac{z_{max}}{2}. \end{aligned} \tag{11}$$

The parallel flow-field with the 2-pass pattern has the largest path-length difference, Δz, but also has a zero Δz at the mid-point of the field ($z = z_{max}/2$). The 3-pass pattern results in a smaller Δz for $z < z_{max}/3$ and $z > 2z_{max}/3$ compared with the 2-pass pattern, but a larger Δz for $z_{max}/2 < z < 2z_{max}/3$. That is, the 3-pass pattern leads to a more uniform distribution of Δz along the channel than does the 2-pass pattern. The distribution of Δz in the parallel flow-fields with the 5-pass (spiral) or 7-pass (spiral) patterns seems to approach that with the 2-pass pattern, doing so, more closely, as the pass number increases.

Fig. 4(b) indicates that the 2-pass pattern results in the most uniform distribution of $\bar{z}^{y\parallel}$ around its mean value of $z_{max}/2$, while the 1-pass pattern results in the most non-uniform distribution. The local-averaged path-length, $\bar{z}^{y\parallel}$, is observed to be more uniform
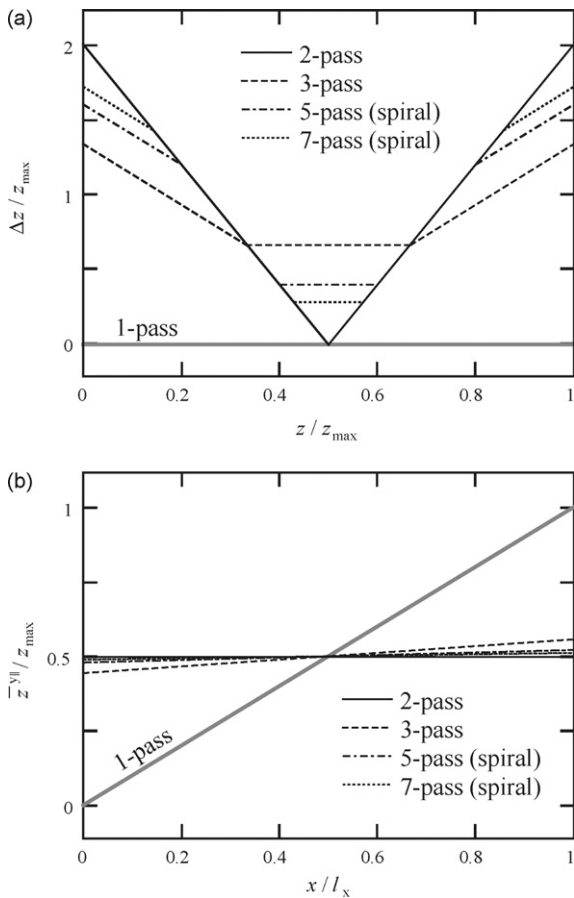
Fig. 4. Geometrical characterization results for basic parallel flow-fields: (a) path-length difference, Δz; (b) local-averaged path-length, $\bar{z}$.

Fig. 5. Design procedure for generating single-path MPSFFs: (a) serpentine master field is designed first, (b) which is divided into several passes according to pass number ($n_{pass} = 3$ for a 3-pass pattern). Finally, (c) proper terminals of separate passes are connected to construct a single-path MPSFF with (d) inner- or (e) edge-located inlet/outlet ports.

Fig. 6. Single serpentine flow-fields generated for small cells with a 9 cm² active area (3×3 cm): (a) conventional serpentine flow-field, (b) MPSFF with a 2-pass pattern, (c) and (d) MPSFFs with a 3-pass pattern, (e) MPSFF with 5-pass (spiral) pattern, and (f) conventional spiral flow-field.

when the pattern is changed from the 3-pass to the 5-pass (spiral) and 7-pass (spiral) pattern. By contrast the differences in $\bar{z}^{y\parallel}$ between all of the multi-pass channel patterns are not noticeable in Fig. 4(b).

3.2. Single-path MPSFFs for small cells

A simple, step-by-step design procedure to generate single-path multi-pass serpentine flow-fields (MPSFFs) is presented in Fig. 5. A master field, through which a selected channel pattern is directed, is designed first, as shown in Fig. 5(a). The unit tile length of the master field, l_{tile}, is predetermined by multiplying the pass number, n_{pass}, of the selected channel pattern by l_{unit} ($l_{tile} = n_{pass} \times l_{unit}$). Then, as shown in Fig. 5(b), the master field is divided into several passes according to n_{pass} ($n_{pass} = 3$ in the Figure). The flow-field obtained at this stage is similar to the conventional parallel serpentine flow-fields. As a final step, proper terminals of those separated passes are connected to form a single long MPSFF, as shown in Fig. 5(c). Note that two different MPSFFs can be generated, as shown in Fig. 5(d) and (e), wherein the positions of the inlet/outlet ports are different (edge or inner).

Six flow-field designs generated for a square active area of 9 cm² (3 cm × 3 cm) are shown in Fig. 6, wherein the channel cells are shaded according to their path-length values. A total of 225 (15 × 15) channel cells with $l_{unit} = 2$ mm were needed to cover the 9 cm² cell area. Fig. 6 shows a conventional serpentine flow-field (small a), a conventional spiral flow-field (small f), and four MPSFFs (small b, c, d, and e) that have been generated according to the proposed design method. The master fields and the selected channel patterns are also provided in Fig. 6.
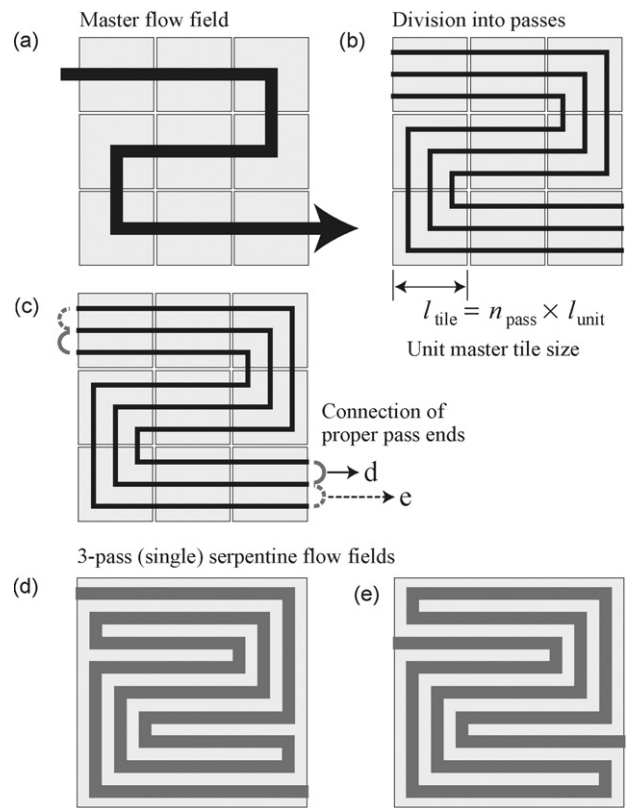
The MPSFF shown in Fig. 6(b) is similar to the flow-field design proposed for coolant flow-fields in prior studies [19,20] to provide better cooling of PEMFCs. Similarly, the MPSFF shown in Fig. 6(c) is almost the same as the convection enhanced serpentine flow-field (CESFF) proposed by Xu and Zhao [18] to improve the performance and stability of DMFCs. The MPSFFs (small b, c, d, and e) and the spiral flow-field (small f) in Fig. 6 share a geometrical characteristic, i.e., the proximal location or the interlaced pattern of channels with dramatically different path-lengths. On the other hand, neighboring channels generally have similar path-lengths in the serpentine flow-field (small a), as indicated in Fig. 6(a).

Fig. 7 shows the path-length difference, Δz, along the channel for the flow-fields shown in Fig. 6. The maximum path-length, z_{max}, is 45 cm (15×3 cm) for the flow-fields. The shaded triangular area in Fig. 7 indicates the regions between the lower and upper boundaries of Δz identified in Fig. 4(a). A relatively small Δz for the serpentine flow-field (small a) can be observed in Fig. 7, which indicates a low under-rib convection in that flow-field. Conversely, the MPSFFs (small b, c, d, and e) are observed to have much larger values of Δz, indicating higher under-rib convection in these flow-fields. The spiral flow-field (small f) has the largest Δz, and thus, the under-rib convection in this flow-field is expected to be the largest.

The path-length difference, Δz, in the MPSFF with the 2-pass pattern (small b) is generally larger than that in the MPSFFs with the 3-pass pattern (small c and d) in Fig. 7, but becomes smaller for $z_{max}/3 < z < 2z_{max}/3$. Thus, the under-rib convection in the MPSFFs with the 3-pass pattern is believed to be more uniform compared with the MPSFF with the 2-pass pattern. The MPSFF with
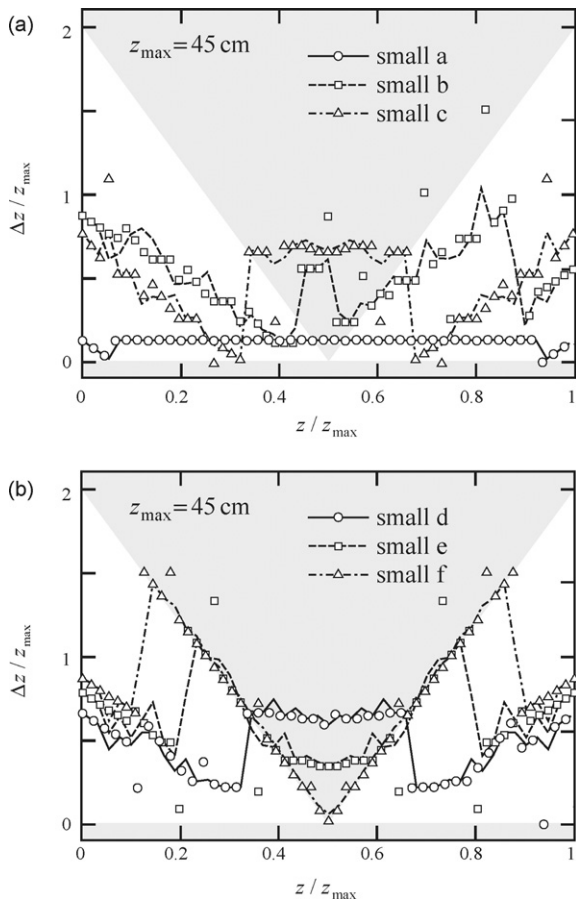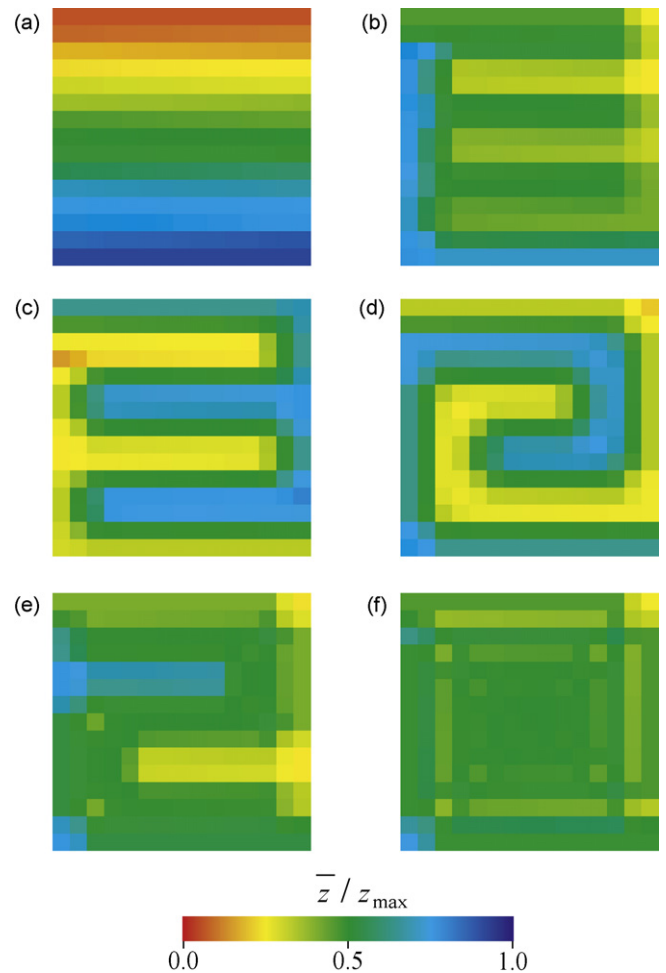
Fig. 8. Spatial distribution of local-averaged path-length, $\bar{z}$, in single serpentine flow-fields: (a) a conventional serpentine flow-field, (b) MPSFF with 2-pass pattern, (c) and (d) MPSFFs with 3-pass pattern, (e) MPSFF with 5-pass (spiral) pattern, and (f) conventional spiral flow-field.

the 5-pass pattern (small e) and the spiral flow-field (small f) have very high values of Δz, but also relatively small values of Δz near the mid-point of $z = z_{max}/2$. This trend is quite similar to the distribution of Δz for the parallel flow-field with the 2-pass pattern shown in Fig. 4(a). The most non-uniform under-rib convection is believed to occur in the spiral flow-field (small f).

The distributions of the local-averaged path-length, $\bar{z}$, for the single-path MPSFFs are presented in Fig. 8. The serpentine flow-field (small a) shows the most non-uniform distribution of $\bar{z}$, while the spiral flow-field (small f) shows the most uniform distribution. Note that the distribution of $\bar{z}$ is generally related to the reactant concentration distribution in the PEMFCs, and also to the temperature distribution in the cooling plates of the PEMFCs. Fig. 8 shows that regions of high and low z are closely-interlaced in the MPSFFs (small b, c, d, and e), thereby leading to a more uniform distribution of $\bar{z}$.

The geometrical characterization indices for the single-path MPSFFs shown in Figs. 6–8 are summarized in Table 2. The average pass-length difference, $(\Delta z)_{avg,1/3}$, for $0 < z < z_{max}/3$ is only about 5.4 cm for the conventional serpentine flow-field (small a), while it is in the range of 17.0–32.9 cm for the MPSFFs (small b, c, d, and e). The spiral flow-field (small f) has the largest $(\Delta z)_{avg,1/3}$ of approximately 44.2 cm. The under-rib convection intensities, q_{rib}/q_{tot}, are also provided in Table 2, which are about 4.6% for the serpentine flow-field, 14.5–28.1% for the MPSFFs, and 37.7% for the spiral flow-field. These values should only be considered as estimates because

Fig. 7. Variation of path-length difference, Δz, along channel in single serpentine flow-fields: (a) for flow-fields of small a, b, and c, and (b) for flow-fields of small d, e, and f.

Table 2
Geometrical characterization indices of single serpentine flow-fields generated for a small active area (3×3 cm).

	Master field	n_{pass}	z_{max} (cm)	$(\Delta z)_{avg,1/3}$ (cm)	$\sigma_{\bar{z}}$ (cm)	$q_{rib,1/3}/q_{tot}$ (%)
Small a	Serpentine (15×15)	1-pass	45	5.4	12.7	4.6
Small b	Serpentine (7×7)	2-pass	45	27.1	6.1	23.1
Small c	Serpentine (5×5)	3-pass	45	17.0	8.4	14.5
Small d	Spiral (5×5)	3-pass	45	18.5	7.5	15.8
Small e	Serpentine (3×3)	5-pass (spiral)	45	32.9	5.3	28.1
Small f	Spiral (15×15)	1-pass	45	44.2	3.6	37.7

of the many simplifying assumptions employed in the derivation of Eq. (9). Nevertheless, q_{rib}/q_{tot} in Table 2 clearly indicates that the MPSFFs can greatly enhance under-rib convection over conventional serpentine flow-fields.

The standard deviation, $\sigma_{\bar{z}}$, of the local-averaged path-length, $\bar{z}$ (whose $(\bar{z})_{avg}$ is 22.5 cm), is also provided in Table 2. This value is related to the spatial uniformity of the operational conditions, as explained above. The serpentine flow-field (small a) has the largest deviation of about 12.7 cm, while the spiral flow-field (small f) has the smallest of approximately 3.6 cm. The MPSFFs (small b, c, d, and e) have $\sigma_{\bar{z}}$ in the range of 5.3–8.4 cm, which indicates better uniformity in operating conditions in the MPSFFs compared with a conventional serpentine flow-field.

3.3. Parallel-path MPSFFs for large cells

A step-by-step procedure to design multi-pass serpentine flow-fields (MPSFFs) having parallel paths is presented in Fig. 9. The similarity between Fig. 5 for the design of single-path MPSFFs and Fig. 9 for parallel-path MPSFFs should be noted. A master field shown in Fig. 9(a) is first divided into several paths according to the number of parallel paths, n_{path} ($n_{path} = 3$ in the Figure), then further into several passes according to n_{pass} (also $n_{pass} = 3$ in the Figure). The intermediate flow-field shown in Fig. 9(c) is the same as the conventional serpentine flow-field with nine parallel paths. Finally, proper terminals of those separated passes are connected to form a MPSFF having parallel paths, as shown in
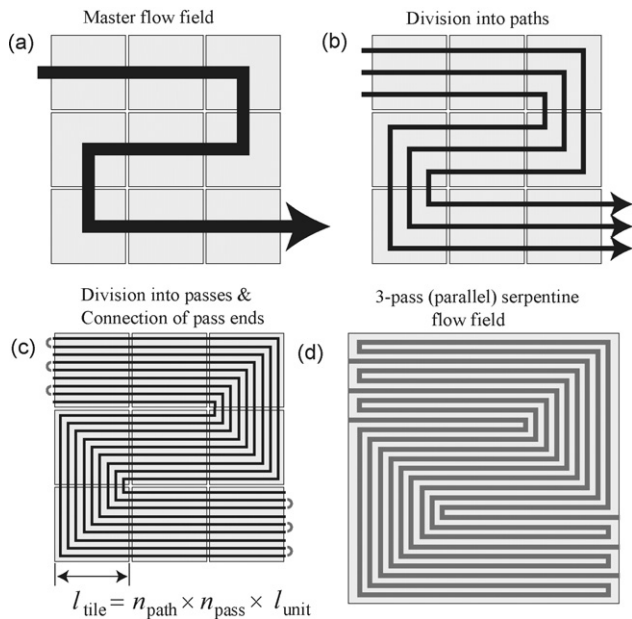
Fig. 9(d). The unit tile length of the master field, l_{tile}, is determined as $l_{tile} = n_{path} \times n_{pass} \times l_{unit}$.

Fig. 10 shows six flow-field designs for a square cell area of 81 cm^2 (9 cm $\times$ 9 cm), with three parallel paths (large a, b, and c)
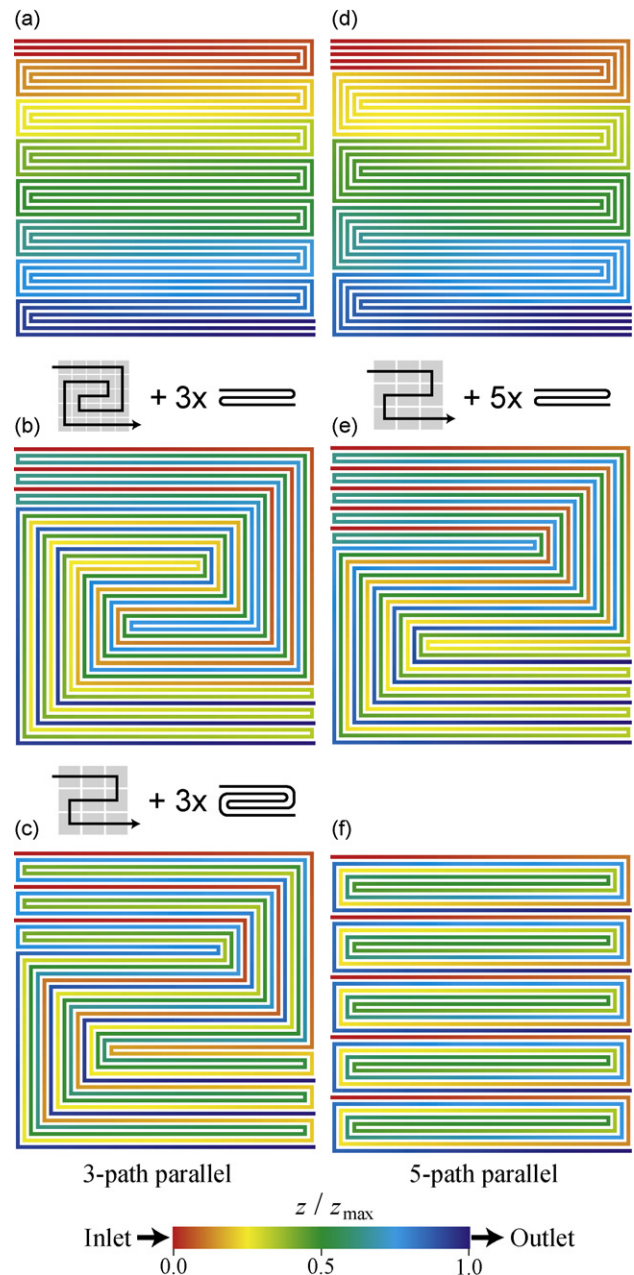
Fig. 10. Parallel serpentine flow-fields generated for large cells with 81 cm^2 active area (9 $\times$ 9 cm): (a) conventional 3-path serpentine flow-field, (b) 3-path MPSFF with 3-pass patterns, (c) 3-path MPSFF with 5-pass patterns, (d) conventional 5-path serpentine flow-field, (e) 5-path MPSFF with 3-pass patterns, (f) 5-path MPSFF with 9-pass spiral patterns.

Fig. 9. Design procedure for generating parallel-path MPSFFs: (a) serpentine master field is designed first, which is divided into several passes according to (b) path number ($n_{path} = 3$ for three parallel paths), and then according to (c) pass number ($n_{pass} = 3$ for 3-pass patterns). Finally, (d) proper terminals of separate passes are connected to construct a parallel-path MPSFF.

or five parallel paths (large d, e, and f). A total of 2025 (45×45) channel cells with $l_{unit} = 2$ mm were required to construct these flow-fields. The maximum path-length, z_{max}, was 135 cm for the 3-path parallel flow-fields (large a, b, and c) and 81 cm for the 5-path parallel flow-fields (large d, e, and f). The total path-length, summing all of the parallel paths, equals 405 cm (45×9 cm). The flow-fields shown in Fig. 10 can be categorized as conventional parallel serpentine flow-fields (large a and d), and parallel-path MPSFFs constructed based on a 3-pass channel pattern (large b and e), a 5-pass spiral pattern (large c) and a 9-pass spiral pattern (large f). Highly-interlaced channel patterns in the parallel-path MPSFFs can clearly be observed in Fig. 10.

The distribution of the path-length difference, Δz, along the channel is illustrated in Fig. 11. The serpentine flow-fields (large a and d) have very small values of Δz. The reason for this trend is because most channels are in contact with channels of similar path-lengths due to the parallel arrangement (see Figs. 10(a) and (d)). The MPSFFs (large b, c, e, and f) have much larger values of Δz compared with the serpentine flow-fields, which suggests that the under-rib convection in these MPSFFs is greatly enhanced. Fig. 11 also shows that the 3-pass pattern leads to a more uniform distribution of Δz than does the 5-pass spiral pattern or the 9-pass spiral pattern. A uniform distribution of Δz is important for obtaining a uniform under-rib convection intensity throughout the flow-field. The similarity between the spiral channel patterns and the 2-pass pattern is, again, demonstrated in Fig. 11, i.e., Δz of the MPSFF with the 9-pass spiral pattern closely follows the upper boundary that has been determined from the parallel flow-field with the 2-pass pattern in Fig. 4(a).
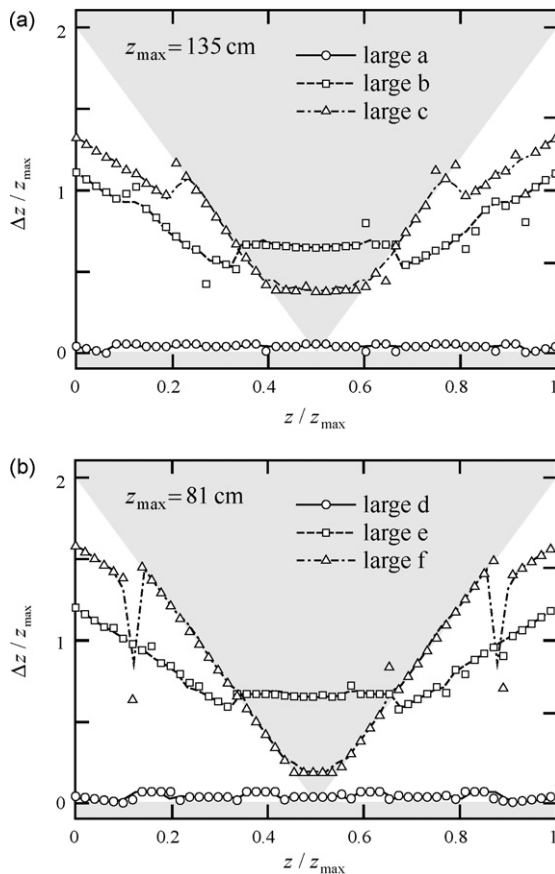

Fig. 12. Spatial distribution of local-averaged path-length, $\bar{z}$, in parallel serpentine flow-fields: (a) conventional 3-path serpentine flow-field, (b) 3-path MPSFF with 3-pass patterns, (c) 3-path MPSFF with 5-pass patterns, (d) conventional 5-path serpentine flow-field, (e) 5-path MPSFF with 3-pass patterns, (f) 5-path MPSFF with 9-pass spiral patterns.

Fig. 12 shows that the local-averaged path-length, $\bar{z}$, is more uniformly distributed in the MPSFFs (large b, c, e, and f) than in the serpentine flow-fields (large a and d), indicating that the operation conditions are expected to be more uniform in the MPSFFs. This also points out that these parallel-path MPSFFs can work well as coolant flow-fields for PEMFCs or DMFCs. Fig. 12 also shows that increasing the parallel path number, n_{path}, enhances the uniformity of the $\bar{z}$ distribution in the cell area.

The geometrical characterization indices for the parallel-path MPSFFs shown in Figs. 10–12 are summarized in Table 3. The MPSFFs (large b, c, e, and f) are observed to have significantly larger average path-length differences, $(\Delta z)_{avg,1/3}$, compared with the serpentine flow-fields (large a and d). The under-rib convection intensity, $q_{rib,1/3}/q_{tot}$, is only about 5.4% or 2.9% for the serpentine flow-fields (large a and d), while it is 278.3% or 109.4% for the MPSFFs with the 3-pass pattern (large b and e). Although a value for $q_{rib,1/3}/q_{tot}$ greater than 100% definitely violates the assumption of a negligible under-rib convection for Eq. (9), such large values of $q_{rib,1/3}/q_{tot}$ clearly point to significantly higher under-rib convections in those parallel-path MPSFFs.

Table 3 indicates that an increase in the path number, n_{path}, from three (large a, b, and c) to five (large d, e, and f) generally decreases

Fig. 11. Variation of path-length difference, Δz, along channel in parallel serpentine flow-fields: (a) for 3-path flow-fields of large a, b, and c, and (b) for 5-path flow-fields of large d, e, and f.
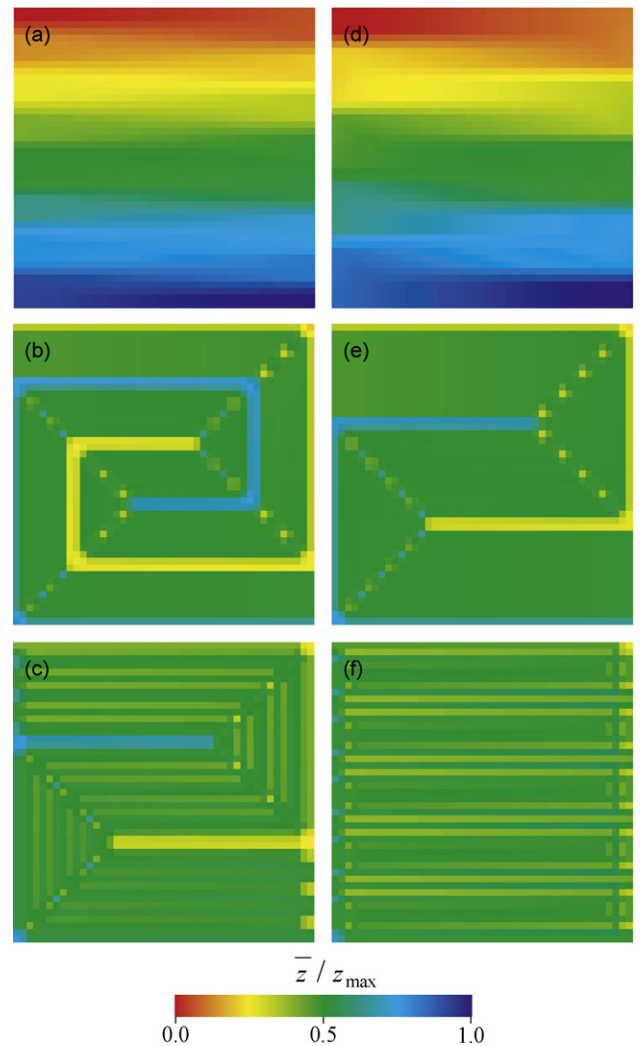
Table 3
Geometrical characterization indices of parallel serpentine flow-fields generated for a large active area (9×9 cm).

	Master field	n_{pass}	n_{path}	z_{max} (cm)	$(\Delta z)_{avg,1/3}$ (cm)	$\sigma_{\bar{z}}$ (cm)	$q_{rib,1/3}/q_{tot}$ (%)
Large a	Serpentine (15×15)	1-pass	3	135	5.4	38.8	13.7
Large b	Spiral (5×5)	3-pass	3	135	108.7	13.2	278.3
Large c	Serpentine (3×3)	5-pass (spiral)	3	135	142.0	10.9	363.7
Large d	Serpentine (9×9)	1-pass	5	81	2.9	23.2	4.5
Large e	Serpentine (3×3)	3-pass	5	81	71.2	6.1	109.4
Large f	Straight (1×1)	9-pass (spiral)	5	81	96.8	6.6	148.8

the under-rib convection intensity. This is explained by the linear proportionality of $q_{rib,1/3}/q_{tot}$ to z_{max} given in Eq. (9). The maximum path-length, z_{max}, is inversely proportional to n_{path}, and so is the under-rib convection intensity, $q_{rib,1/3}/q_{tot}$. Comparison of the MPSFF with the 3-pass pattern (large b) and with the 5-pass spiral pattern (large c) reveals that spiral patterns generally result in higher under-rib convection intensities, which is consistent with the result of Fig. 4(a).

Table 3 also suggests that the standard deviation, $\sigma_{\bar{z}}$, of the $\bar{z}$ distribution in the active area is significantly reduced from about 38.8 or 23.2 cm in the serpentine flow-fields (large a and d) to about 13.2 or 6.1 cm in the MPSFFs with the 3-pass pattern (large b and e). The reduction of $\sigma_{\bar{z}}$ by a factor of approximately 1/3 indicates that parallel-path MPSFFs are favourable for the uniformity of the local-averaged path-length, $\bar{z}$, and thus also for the uniformity of operating conditions. The inverse proportionality of $\sigma_{\bar{z}}$ to the number of parallel paths, n_{path}, can also be observed in Table 3.

4. Discussion

This study focuses on increasing the path-length difference, Δz, in serpentine flow-fields with the hypothesis that an enhancement of under-rib convection between neighbouring channels improves the performance of PEMFCs. The results of Xu and Zhao [18] and Qi and Kaufman [22] support the favourable effects of under-rib convection enhancement on PEMFC performance. On the other hand the negative effects of enhanced under-rib convection have also been addressed by Rock [27], who proposed mirrored serpentine flow-field designs for fuel cells and suggested that the performance of PEMFCs could be improved by reducing the cross-leakage flow or bypass flow in the flow-fields. The terms cross-leakage and bypass flow denote the same process as under-rib convection. These seemingly controversial results concerning under-rib convection in serpentine flow-fields may be explained by the difference in the cell sizes considered in those studies [18,22,27].

The path-length difference, Δz, of conventional serpentine flow-fields is directly determined by the cell size. For example, a serpentine flow-field for an L cm $\times L$ cm active area has an average path-length difference, $(\Delta z)_{avg}$, of $2L$. Thus, $(\Delta z)_{avg}$ in the serpentine flow-field is only about 6 cm for small cells having a 3 cm $\times$ 3 cm active area. Recalling that the under-rib convection intensity is proportional to the path-length difference, it is well understood that small cells, such as the one considered by Xu and Zhao [18], can perform better when the under-rib convection is enhanced; however, large cells, such as the 20 cm $\times$ 24 cm cell considered in Shimpalee et al. [28] (based on the design of Rock [27]), have a large $(\Delta z)_{avg}$ of about 40 cm, and thus, already have a high under-rib convection intensity. As pointed out in Rock [27], excessive under-rib convection in serpentine flow-fields can result in premature exhaust of reactant gases due to the flow short-circuiting. This bypass flow through the under-rib region also reduces the flow speed in the channel, which adversely impacts reactant distribution and liquid water transport. In this case, higher performance is achieved by regulating the excessive under-rib convection in PEMFCs.

The MPSFFs proposed in this study provide a way to maximize the path-length difference, and thus, the under-rib convection in a given cell area. Based on the above discussion, MPSFFs are expected to be more advantageous for small fuel cells primarily employed for portable applications. The enhanced under-rib convection in MPSFFs decreases the pressure drop across PEMFCs, which also contributes to the performance by reducing the power consumption of air blowers in portable systems. More uniform distributions of reactant concentration, temperature and liquid water saturation are another advantage of MPSFFs, which enable better control of PEMFC operation, as well as the use of dry reactant gases with internal humidification. The MPSFFs are also expected to be useful to achieve better uniformity in coolant flow-fields for PEMFCs.

This study geometrically characterized single- and parallel-path MPSFFs based on the path-length, z, and estimated the under-rib convection intensities in the flow-fields. Nevertheless, the exact effects of the enhanced under-rib convection on the performance of PEMFCs still need to be clarified through further numerical and experimental investigations. For this purpose, the authors are currently working on numerical studies to determine the flow distribution, pressure drop, and cooling characteristics of the proposed MPSFFs.

5. Summary

A simple, step-by-step design method to generate single- and parallel-path multi-pass serpentine flow-fields (MPSFFs) for PEMFC applications is presented in this study. MPSFFs comprised of multi-pass flow channels arranged in serpentine configurations allow channels with widely different path-lengths to be positioned near one another. The resulting maximum path-length difference between neighbouring flow-channels is expected to enhance under-rib convection and transport, thereby improving the performance of PEMFCs. In addition, the highly-interlaced channel patterns in MPSFFs are expected to improve the uniformity of local conditions, such as reactant and product concentrations, temperature and liquid water saturation in the active cell area. Several single- and parallel-path MPSFFs generated by the proposed design method have also been presented, along with the results of their geometrical characterization. The implication of under-rib convection enhancement on the performance of PEMFCs with different cell sizes has also been discussed.

References

[1] J. Larminie, A. Dicks, Fuel Cell Systems Explained, John Wiley & Sons, Chichester, 2000.
[2] R.P. O'Hayre, S.W. Cha, W. Colella, F.B. Prinz, Fuel Cell Fundamentals, John Wiley & Sons, New York, 2006.
[3] A. Faghri, Z. Guo, Int. J. Heat Mass Transfer 48 (2005) 3891–3920.
[4] X. Li, I. Sabir, Int. J. Hydrogen Energy 30 (2005) 359–371.
[5] T.V. Nguyen, J. Electrochem. Soc. 143 (1996) L103–L105.
[6] W. He, J.S. Yi, T.V. Nguyen, AIChE J. 46 (1999) 2053–2064.
[7] S. Dutta, S. Shimpalee, J.W. Van Zee, Int. J. Heat Mass Transfer 44 (2001) 2029–2042.
[8] M.V. Williams, E. Begg, L. Bonville, H.R. Kunz, J.M. Fenton, J. Electrochem. Soc. 151 (2004) A1173–A1180.
[9] M.V. Williams, H.R. Kunz, J.M. Fenton, J. Electrochem. Soc. 151 (2004) A1617–A1627.
[10] J.G. Pharoah, J. Power Sources 144 (2005) 77–82.
[11] P.H. Oosthuizen, L. Sun, K.B. McAuley, Appl. Therm. Eng. 25 (2005) 1083–1096.
[12] L. Sun, P.H. Oosthuizen, K.B. McAuley, Int. J. Therm. Sci. 45 (2006) 1021–1026.

[13] J.P. Feser, A.K. Prasad, S.G. Advani, J. Power Sources 161 (2006) 404–412.
[14] Q. Ye, T.S. Zhao, C. Xu, Electrochim. Acta 51 (2006) 5420–5429.
[15] T. Kanezaki, X. Li, J.J. Baschuk, J. Power Sources 162 (2006) 415–425.
[16] J. Park, X. Li, J. Power Sources 163 (2007) 853–863.
[17] K.B.S. Prasad, S. Jayanti, J. Power Sources 180 (2008) 227–231.
[18] C. Xu, T.S. Zhao, Electrochem. Commun. 9 (2008) 497–503.
[19] F.C. Chen, Z. Gao, R.O. Loutfy, M. Hecht, Fuel Cells 3 (2003) 181–188.
[20] J. Choi, Y.H. Kim, Y. Lee, K.J. Lee, Y. Kim, J. Mech. Sci. Tech. 22 (2008) 1417–1425.
[21] A. Kaufman, P.L. Terry, US Patent (1998) #5,776,625.
[22] Z. Qi, A. Kaufman, J. Power Sources 109 (2002) 469–476.
[23] M. Kaviany, Principles of Heat Transfer in Porous Media, 2nd ed., Springer, New York, 1999.
[24] B.R. Munson, D.F. Young, T.H. Okiishi, Fundamentals of Fluid Mechanics, 5th ed., John Wiley & Sons, New York, 1999.
[25] J.T. Gostick, M.W. Fowler, M.D. Pritzker, M.A. Ioannidis, L.M. Behra, J. Power Sources 162 (2006) 228–238.
[26] J.P. Feser, A.K. Prasad, S.G. Advani, J. Power Sources 162 (2006) 1226–1231.
[27] J.A. Rock, US Patent (2000) #6,099,984.
[28] S. Shimpalee, S. Greenway, D. Spuckler, J.W. Van Zee, J. Power Sources 135 (2004) 79–87.